INTERNATIONAL JOURNAL FOR NUMERICAL METHODS IN FLUIDS
Int. J. Numer. Meth. Fluids 2008; **00**:1–6 *Prepared using* fldauth.cls *[Version: 2002/09/18 v1.01]*

An EBE finite element method for simulating nonlinear flows in rotating spheroidal cavities

K. H. Chan[1], K. Zhang[2*], and X. Liao[3]

[1] *Department of Mathematics, The University of Hong Kong, Pokfulam, Hong Kong*
[2] *Department of Mathematical Sciences, University of Exeter, EX4 4QE, UK*
[3] *Shanghai Astronomical Observatory, Chinese Academy of Sciences, Shanghai 200030, China*

SUMMARY

Many planetary and astrophysical bodies are rotating rapidly, fluidic and, as a consequence of rapid rotation, in the shape of an ablate spheroid. We present an efficient EBE (Element-By-Element) finite element method for the numerical simulation of nonlinear flows in rotating incompressible fluids that are confined in an ablate spheroidal cavity with arbitrary eccentricity. Our focus is placed on temporal and spatial tetrahedral discretization of the EBE finite element method in spheroidal geometry, the EBE parallelization scheme and the validation of the nonlinear spheroidal code via both the constructed exact nonlinear solution and a special resonant forcing in the inviscid limit.

KEY WORDS: Finite Element Method; Spheroids; Rotation

1. INTRODUCTION

There are many geophysical and astrophysical systems that share the three common characters: they are fluidic, rotating rapidly and in spheroidal shape. Planet Earth spins fast and its interior consists of molten iron that is confined in a spheroidal cavity defined by the core-mantle boundary [10]. It was conjectured that the spheroidal shape of the Earth's fluid interior, together with the lunar-solar precession, may be responsible for generating and maintaining the geomagnetic field [4]. This conjecture has been supported not only by laboratory experiments demonstrating wavelike instabilities and the transition to complex turbulent flows can occur in rotating spheroids [18, 31, 20] but also by numerical experiments showing that procession-driven flows can generate and sustain magnetic fields [29, 15, 28]. Many early-type stars, because of their rapid rotation, are also in the shape of a Roche spheroid in which the effect of rapid rotation induces both the geometric flattening and latitudinal variation of the temperature [23]. Furthermore, the shape of galaxy may be treated as a highly flatted spheroid with a large eccentricity [32]. It follows that, in addition to intrinsic mathematic

*Correspondence to: kzhang@ex.ac.uk

interest in the spheroidal problem [27, 24], an efficient numerical method for the problem of fluid dynamics in rotating ablate spheroidal cavities has many important applications in geophysics and astrophysics.

The problem of fluid dynamics in spheroidal geometry is, however, mathematically and computationally less tractable than that for spherical geometry. Spectral methods based on spherical harmonic expansions have been widely and conveniently employed in the numerical studies of convection and dynamos in rotating spherical systems (e.g., [34, 12, 25, 29]). In the framework of spherical spectral approximations, the flow velocity $\mathbf{u}$ for a Boussinesq or an anelastic fluid may be expressed as a sum of poloidal (v) and toroidal (w) vectors

$$\rho_0(\mathbf{r})\,\mathbf{u}(\mathbf{r},t) = \nabla\times\nabla\times[\mathbf{r}v(\mathbf{r},t)] + \nabla\times[\mathbf{r}w(\mathbf{r},t)], \tag{1}$$

where $\mathbf{r}$ is the position vector, ρ_0 is the density distribution depending on $\mathbf{r}$ only or being constant, and the modified solenoidal condition $\nabla\cdot(\rho_0\mathbf{u}) = 0$ is automatically satisfied at the expense of raising the order of governing partial differential equations. The poloidal (v) and toroidal (w) functions are then further expanded in the form

$$v(\mathbf{r},t) = \sum_{m,l}\left[\hat{v}_{lm}(t)\; v_{lm}(r)\, Y_l^m(\theta,\phi) + c.c.\right], \tag{2}$$

$$w(\mathbf{r},t) = \sum_{m,l}\left[\hat{w}_{lm}(t)\; w_{lm}(r)\, Y_l^m(\theta,\phi) + c.c.\right], \tag{3}$$

where *c.c.* denotes the complex conjugate of the preceding term, $v_{lm}(r)$ and $w_{lm}(r)$ are a function of r satisfying the required boundary condition on the bounding surface of a spherical cavity, and $Y_l^m(\theta,\phi)$ is the spherical harmonics of degree l. For the spherical problem, the boundary geometry of the container is automatically consistent with the nature of spherical polar coordinates, and, consequently, the spectral mathematical formulation/implementation is straightforward. Spheroidal boundary geometry, however, cannot be accommodated by spherical polar coordinates and, as a result, either a coordinate transformation that maps the spheroidal domain into the spherical domain [17] or complicated oblate spheroidal coordinates [26] must be used in the spectral approximation for nonlinear flows confined in spheroidal cavities. A major numerical disadvantage of the spheroidal spectral method, in addition to the fact that the Legendre transform is computationally inefficient and severely limits the effectiveness of the method on modern parallel computers, is that the coordinate transformation or oblate polar spheroidal coordinates must lead to more complicated governing equations that make numerical implementation more difficult. Moreover, there apparently exist numerical instabilities in the spheroidal spectral approximation using spherical harmonics when the eccentricity of a rotating spheroid ε is high, $\varepsilon \geq 0.6$ [26]. It is hence desirable to find an alternative numerical method, which is non-spectral and can be readily implemented on modern parallel computers, for efficiently solving the problem of fluid dynamics in rotating spheroids.

In this study, we present an EBE (Element-By-Element) finite element method that can be effectively used for the numerical simulation of nonlinear flows confined in a rotating spheroidal cavity with arbitrary eccentricity. The EBE finite element method was first successfully employed in simulating convection and dynamos in spherical geometry [5], showing that the EBE scheme can take the full advantage of modern massively parallel computers achieving nearly linear scalability. This study extends the previous spherical work to general spheroidal

geometry by focusing on three different aspects of the finite element approximation for a rotating incompressible fluid confined in spheroidal cavities. First, we shall describe temporal discretization and spatial tetrahedral discretization of the EBE finite element method suitable for general spheroidal geometry. Second, we shall discuss an EBE parallelization scheme suitable for modern massively parallel computers. Finally, we shall validate our nonlinear spheroidal code via two different ways: (i) by constructing an exact nonlinear solution of the spheroidal system we investigate the accuracy and convergence of the spheroidal code, and (ii) by constructing a special resonant forcing we check the numerical solution of the spheroidal code for a small Ekman number against the theoretical prediction in the inviscid limit.

In what follows we shall begin by presenting the mathematical formulation of the numerical problems in §2. The EBE finite element method is discussed in §3. Numerical results are presented in §4 and the paper closes in §5 with a brief summary and concluding remarks.

2. MATHEMATICAL FORMULATION OF THE NUMERICAL PROBLEM

Consider an impressible fluid of kinematic viscosity ν contained in an oblate spheroidal cavity whose bounding surface is defined by

$$\left(\frac{x^*}{a}\right)^2+\left(\frac{y^*}{b}\right)^2+\left(\frac{z^*}{c}\right)^2=1 \tag{4}$$

where $a=b$ denotes the major axe of an oblate spheroid, c with $c<a$ is the minor axe of the oblate spheroid and the z^*-axis is parallel to the axis of rotation. An important parameter describing the geometry of an oblate spheroid is its eccentricity defined as

$$\varepsilon=\sqrt{\frac{a^2-c^2}{a^2}},\quad 0<\varepsilon<1. \tag{5}$$

The limit $\varepsilon\to 0$ corresponds to the special case for a sphere while the limit $\varepsilon\to 1$ corresponds to a flatted spheroidal disk. The problem of fluid dynamics in a rotating oblate spheroidal cavity, driven by an external force $\mathbf{f}^*(\mathbf{x}^*,t^*)$, which may, for example, arise from the effect of precession or nutation or libration, is governed by the equations

$$\frac{\partial\mathbf{u}^*}{\partial t^*}+\mathbf{u}^*\cdot\nabla\mathbf{u}^*+2\boldsymbol{\Omega}\times\mathbf{u}^*=-\frac{1}{\rho}\nabla p^*+\nu\nabla^2\mathbf{u}^*+\mathbf{f}^*(\mathbf{x}^*,t^*), \tag{6}$$

$$\nabla\cdot\mathbf{u}^*=0, \tag{7}$$

where $\boldsymbol{\Omega}$ represents the angular velocity of the spheroidal container, p^* is the total pressure, $\mathbf{u}^*$ is the three-dimensional velocity field and $\mathbf{f}^*$ denotes external forces such as the Poincaré force.

Employing a as the length scale, Ω^{-1} as the unit of time and $\rho a^2\Omega^2$ as the unit of pressure, while the bounding surface of the spheroidal container is described by the dimensionless equation

$$x^2+y^2+\frac{z^2}{1-\varepsilon^2}=1, \tag{8}$$

the sketch of which is depicted in Fig. 1, the numerical problem is governed by the dimensionless equations

$$\frac{\partial\mathbf{u}}{\partial t}+\mathbf{u}\cdot\nabla\mathbf{u}+2\hat{\mathbf{z}}\times\mathbf{u}=-\nabla p+E\nabla^2\mathbf{u}+\mathbf{f}(\mathbf{x},t), \tag{9}$$

$$\nabla \cdot \mathbf{u} = 0, \tag{10}$$

where $\hat{\mathbf{z}}$ is a unit vector parallel to the axis of rotation. For a given non-dimensional forcing $\mathbf{f}$, the mathematical problem is characterized by the geometrical eccentricity ε of a spheroid and by the non-dimensional parameter, the Ekman number E, defined as

$$E = \frac{\nu}{\Omega a^2},$$

measuring the relative importance of viscous to Coriolis forces. Since planets and stars in the shape of spheroid rotate rapidly, we shall focus our numerical studies on small Ekman number $E \ll 1$.

In the present study, the nonlinear problem governed by (9) and (10) in rotating spheroidal cavities subject to a given forcing $\mathbf{f}$ will be solved numerically using an EBE finite element method that is particularly suitable for modern massively parallel computers. In our numerical analysis, we shall adopt the general boundary condition,

$$\mathbf{u}|_{\Sigma} = \boldsymbol{\psi}(\Sigma, t), \tag{11}$$

where the boundary value $\boldsymbol{\psi}(\Sigma, t)$ is assumed to be continuous on the bounding surface Σ of a spheroidal cavity. In order to handle an exact solution $\mathbf{u}_e$ with non-zero divergence, in connection with a possible extension to compressible fluids, we shall present our EBE finite element scheme in §2 for a generalized equation (10) as

$$\nabla \cdot \mathbf{u} = g(\mathbf{x}, t). \tag{12}$$

It should be pointed out that the primary objective of this study is not to understand any particular physical phenomenon taking place in rotating spheroidal fluid systems but to design and validate an effective numerical method that can be employed for the geophysical and astrophysical fluid problem requiring spheroidal geometry. As noted by Lorenzani and Tilgner [17], there exist few analytical or numerical nonlinear solutions for comprehensively validating a nonlinear spheroidal code. We have chosen two different ways of validating our nonlinear spheroidal code. First, we construct an exact nonlinear solution, $\mathbf{u}_e$, of the system and, then, compare $\mathbf{u}_e$ with the corresponding numerical solution computed from the spheroidal code. This comparison not only validates the numerical code but also reveals the important information about the accuracy and convergence of the finite element approximation. Second, we shall derive an analytical solution, $\mathbf{u}_a$, in a rapidly rotating fluid spheroid with arbitrary eccentricity in the limits $\nu \to 0$ and $\mathbf{f} \to 0$ for the small-amplitude flow. By choosing a special forcing $\mathbf{f}(\mathbf{x}, t)$ that corresponds to the solution $\mathbf{u}_a$ at the double limits, we can further check our nonlinear spheroidal code by examining the theoretically predicted resonance at $E \ll 1$.

3. AN EBE FINITE ELEMENT METHOD

3.1. Temporal discretization

Let $t_{\max}$ be a fixed final time of a numerical simulation for the problem of fluid dynamics in a rotating spheroid. We divide the time interval $[0, t_{\max}]$ into M equally spaced subintervals using the following nodal points

$$0 = t_0 < t_1 < t_2 < \ldots < t_M = t_{\max},$$

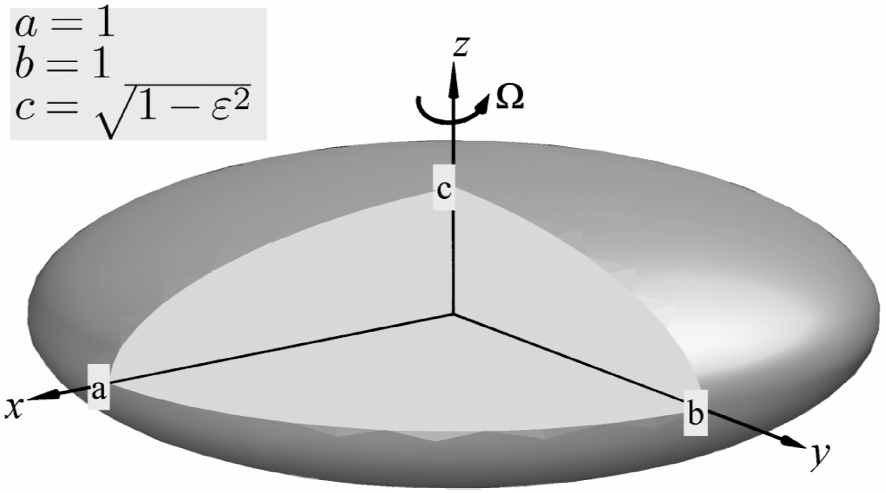

Figure 1. Geometry of a rotating ablate spheroid with eccentricity ε and the z-axis being parallel to the axis of rotation.

where $t_n = n\Delta t$ for $n = 0, 1, \ldots, M$ and $\Delta t = t_{\max}/M$. If $y(\mathbf{r}, t)$ is a function continuous with respect to t, we shall often write $y^n(\mathbf{r}) = y(\mathbf{r}, t_n)$ for $n = 0, 1, \ldots, M$. A semi-implicit time stepping scheme [13, 14] is employed for the time advancement of numerical integration. Firstly an implicit second-order backward differentiation formula (BDF-2) is used for the time derivative, i.e.,

$$\left(\frac{\partial y}{\partial t}\right)^{n+1} = \frac{3y^{n+1} - 4y^n + y^{n-1}}{2\Delta t} + O(\Delta t^2). \tag{13}$$

A second-order extrapolation is applied to the nonlinear term $\mathbf{u}\cdot\nabla\mathbf{u}$. More precisely, the term $\mathbf{u}\cdot\nabla\mathbf{u}$ at $t = t_{n+1}$ is expressed as

$$\mathbf{u}^{n+1}\cdot\nabla\mathbf{u}^{n+1} = 2(\mathbf{u}^n\cdot\nabla\mathbf{u}^n) - (\mathbf{u}^{n-1}\cdot\nabla\mathbf{u}^{n-1}) + O(\Delta t^2). \tag{14}$$

Moreover, we introduce the notation

$$\overline{\overline{\mathbf{u}^{n+1}\cdot\nabla\mathbf{u}^{n+1}}} \equiv 2(\mathbf{u}^n\cdot\nabla\mathbf{u}^n) - (\mathbf{u}^{n-1}\cdot\nabla\mathbf{u}^{n-1}) \tag{15}$$

to simplify the lengthy mathematical expression. A semi-implicit discretization of the governing equations (9) and (10)/(12) in time is: for $n \geqslant 1$, find $\mathbf{u}^{n+1}$ and p^{n+1} such that

$$\frac{3\mathbf{u}^{n+1} - 4\mathbf{u}^n + \mathbf{u}^{n-1}}{2\Delta t} - E\nabla^2\mathbf{u}^{n+1} + 2\hat{\mathbf{z}}\times\mathbf{u}^{n+1} + \nabla p^{n+1} = \mathbf{f}^{n+1} - \overline{\overline{\mathbf{u}^{n+1}\cdot\nabla\mathbf{u}^{n+1}}}, \tag{16}$$

$$\nabla\cdot\mathbf{u}^{n+1} = g^{n+1}. \tag{17}$$

To compute $\mathbf{u}^1$ and p^1 initially, an implicit first-order backward differentiation formula (BDF-1), i.e., a backward Euler scheme, with a first-order extrapolation is used. This procedure is

described by

$$\frac{\mathbf{u}^1 - \mathbf{u}^0}{\Delta t} - E\nabla^2\mathbf{u}^1 + 2\hat{\mathbf{z}} \times \mathbf{u}^1 + \nabla p^1 = \mathbf{f}^1 - \mathbf{u}^0 \cdot \nabla\mathbf{u}^0, \tag{18}$$

$$\nabla \cdot \mathbf{u}^1 = g^1. \tag{19}$$

Although a fixed time-step approach is adopted in the current model, a variable time-step scheme can be readily implemented.

3.2. Spatial discretization

3.2.1. Spheroidal tetrahedral mesh The essential strategy for generating a tetrahedral mesh suitable for spheroidal geometry is first to construct a spherical tetrahedral mesh [7] which is then deformed into a spheroidal tetrahedral mesh by introducing eccentricity ϵ as a geometric parameter of the spheroidal mesh. More precisely, all nodes (x_i, y_i, z_i) for a spherical tetrahedral mesh within the unit sphere satisfying

$$x_i^2 + y_i^2 + z_i^2 = r_i^2, \qquad 0 < r_i \leq 1,$$

can be transformed by

$$x_i^\varepsilon = x_i, \quad y_i^\varepsilon = y_i, \quad z_i^\varepsilon = z_i\sqrt{1-\varepsilon^2}$$

such that the deformed nodes $(x_i^\varepsilon, y_i^\varepsilon, z_i^\varepsilon)$ satisfy

$$(x_i^\varepsilon)^2 + (y_i^\varepsilon)^2 + \frac{(z_i^\varepsilon)^2}{1-\varepsilon^2} = r_i^2, \qquad 0 < r_i \leq 1.$$

If required, we can place more nodes near the bounding surface of a spheroidal cavity by stretching the spherical mesh points (x_i, y_i, z_i) radially before the deformation, for example,

$$\begin{bmatrix} x_i \\ y_i \\ z_i \end{bmatrix} = \frac{1}{r_i}\sin\left(\frac{\pi}{2}r_i\right)^{2/3}\begin{bmatrix} x_i \\ y_i \\ z_i \end{bmatrix}.$$

The spherical mesh begins with approximating the sphere by an icosahedron which is then further divided into 20 identical tetrahedra based on it's 20 triangular facets and the center of the sphere as shown in Fig. 2(a). This initial tetrahedral mesh is then refined recursively by subdividing each of the tetrahedra into eight subtetrahedra according to the method of Liu and Joe [16]. A typical decomposition is illustrated in Fig. 3. The third refinement with 10,240 tetrahedra is displayed in Fig. 2(b).

In this way, the three-dimensional tetrahedralization of the spheroid produces a nearly uniform mesh distribution on the spheroidal surface without the pole problem and a small number of nodes with a nearly uniform mesh distribution in the neighborhood of the center $\mathbf{r} = 0$ without the origin problem. A spheroid ($\varepsilon = 0.95$) filled with 10,240 tetrahedra is illustrated in Fig. 4. When ε is very close to 1, representing a highly flatted spheroidal disk, an alternative meshing algorithm should be used. This is because a regular shaped tetrahedron after transformation may become too stretched and, consequently, lead to a poor finite element approximation. In this case, a general mesh generation algorithm based on the Delaunay triangulation can be employed instead, for example, see Persson and Strang [21].

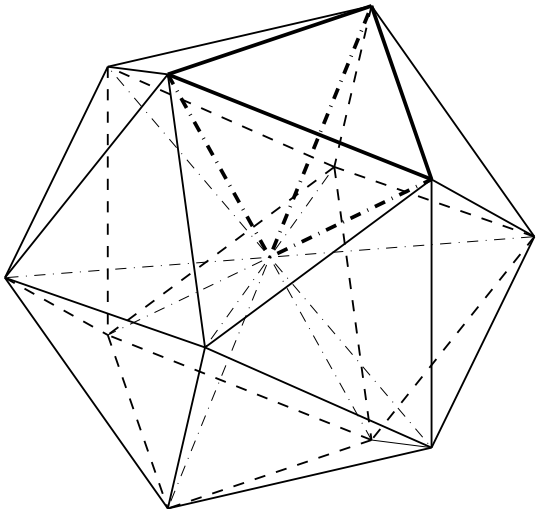

(a)

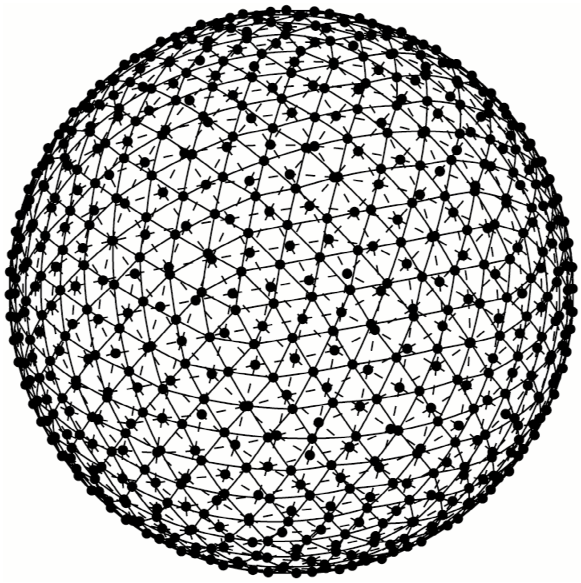

(b)

Figure 2. The unit sphere meshes: (a) the initial mesh showing 12 nodes on a spherical surface with 20 tetrahedra within the sphere and (b) the third refinement showing $2,562$ nodes on a spherical surface with $10,240 = 20 \times 8^3$ tetrahedra within the sphere.

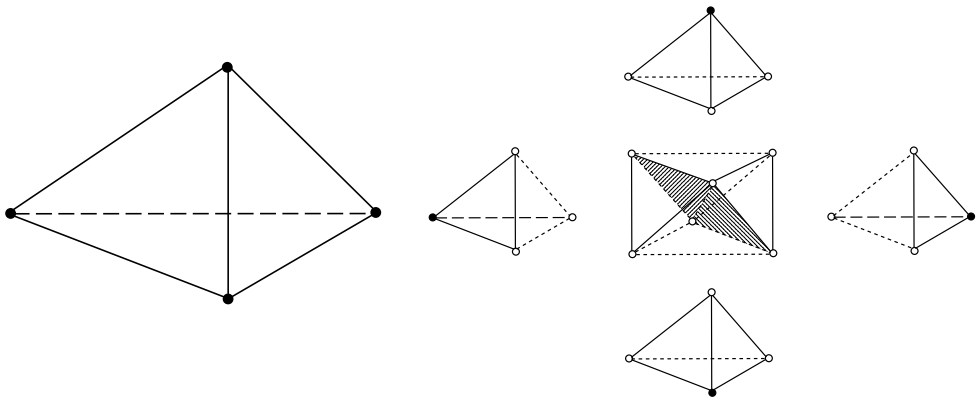

(a) (b)

Figure 3. Subdivision of a tetrahedron into eight subtetrahedra. (a) An original tetrahedron. (b) A typical decomposition into eight subtetrahedra where four of them are at the corners of the original tetrahedron and the other four come from further subdivision of the central octahedron into four subtetrahedra by adding an interior edge.

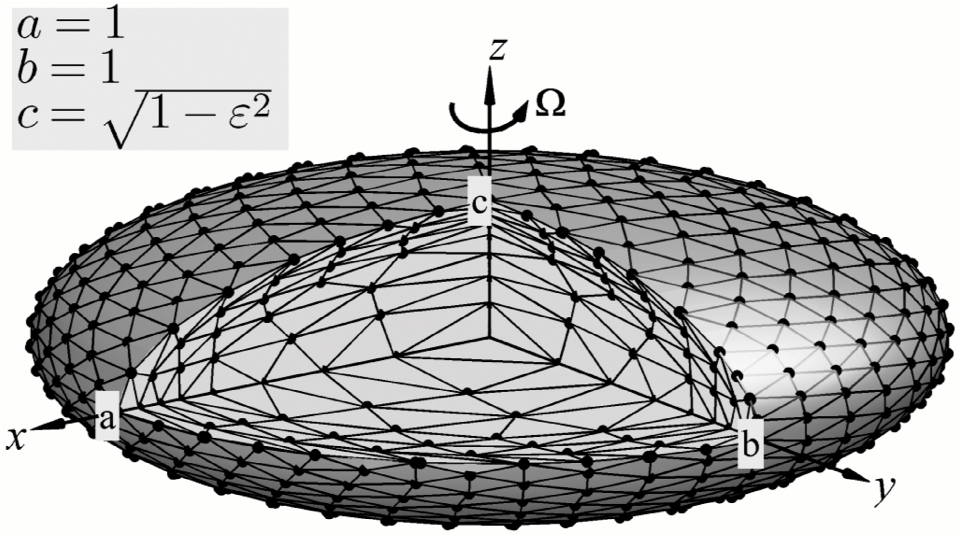

Figure 4. A spheroidal mesh $\varepsilon = 0.95$ with 10,240 tetrahedra showing more nodes being placed in the vicinity of the bounding surface of the spheroid. The region $x > 0, y > 0$ and $z > 0$ is cut off.

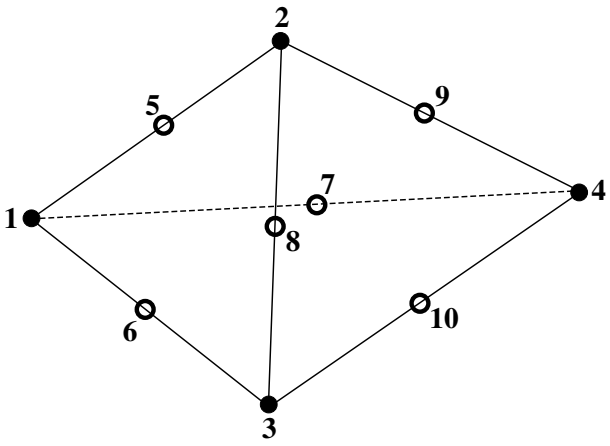

Figure 5. A tetrahedral element: nodes 1 to 4 for the pressure p, nodes 1 to 10 for the velocity $\mathbf{u}$.

3.2.2. Finite element approximation The Galerkin weighted residual approach is adopted in the finite element formulation of the governing equations. Let V denote the spheroidal volume. Multiplying the time discretized equations (16) and (17) by the corresponding weight functions $\mathbf{w_u}$ and w_p, respectively, and then integrating the resulting equations over the region V with appropriate integration by parts, we derive the weak formulation of the governing equations (9) and (12) at time t_{n+1}:

$$\begin{aligned}
&\int_V \left(\frac{3\mathbf{u}^{n+1} - 4\mathbf{u}^n + \mathbf{u}^{n-1}}{2\Delta t}\right) \cdot \mathbf{w_u}\,\mathrm{d}V + \int_V E\nabla\mathbf{u}^{n+1} \cdot \nabla\mathbf{w_u}\,\mathrm{d}V \\
&\quad + \int_V 2\hat{\mathbf{z}} \times \mathbf{u}^{n+1} \cdot \mathbf{w_u}\,\mathrm{d}V + \int_V \nabla p^{n+1} \cdot \mathbf{w_u}\,\mathrm{d}V \qquad (20)\\
&= \int_V \left(\mathbf{f}^{n+1} - \overline{\overline{\mathbf{u}^{n+1} \cdot \nabla\mathbf{u}^{n+1}}}\right) \cdot \mathbf{w_u}\,\mathrm{d}V, \\
&\int_V \left(\nabla \cdot \mathbf{u}^{n+1}\right) w_p\,\mathrm{d}V = \int_V g^{n+1} w_p\,\mathrm{d}V, \qquad (21)
\end{aligned}$$

where the surface integral in Eq. (20) vanishes because the weight functions $\mathbf{w_u}$ is zero on the bounding surface Σ of a spheroid.

The weak formulation (20) and (21) is of the saddle-point form. Mixed finite element of the Hood-Taylor type [11] is used for their spatial discretization. This choice verifies the discrete inf-sup condition, which ensures the existence and uniqueness of the discrete saddle-point problem. The pressure p^{n+1} is uniquely determined up to an additive constant. An additional condition $p^{n+1}(\mathbf{r}_0) =$ constant is imposed at a selected point $\mathbf{r}_0$ numerically. Hood-Taylor elements use the piecewise quadratic polynomials to approximate the velocity $\mathbf{u}$, but use the piecewise linear polynomials to approximate the pressure p. In consequence, there are four nodes for p and ten nodes for $\mathbf{u}$ in each tetrahedron as shown in Fig. 5. On a typical kth

tetrahedral element, we seek approximations for the velocity $\mathbf{u}$ and pressure p by

$$\mathbf{u}^{(k)} = \sum_{j=1}^{10} \mathbf{u}_j^{(k)} N_j^{(k)}, \qquad p^{(k)} = \sum_{j=1}^{4} p_j^{(k)} M_j^{(k)}, \tag{22}$$

where $\mathbf{u}_j^{(k)}$ and $p_j^{(k)}$ are the values of $\mathbf{u}$ and p at the node j. The linear and quadratic shape functions for the kth tetrahedron, $M_j^{(k)}$ and $N_j^{(k)}$, are defined as

$$\begin{aligned}
&M_1^{(k)} = L_1^{(k)}, M_2^{(k)} = L_2^{(k)}, M_3^{(k)} = L_3^{(k)}, M_4^{(k)} = L_4^{(k)};\\
&N_1^{(k)} = L_1^{(k)}(2L_1^{(k)} - 1), N_2^{(k)} = L_2^{(k)}(2L_2^{(k)} - 1), N_3^{(k)} = L_3^{(k)}(2L_3^{(k)} - 1),\\
&N_4^{(k)} = L_4^{(k)}(2L_4^{(k)} - 1), N_5^{(k)} = 4L_1^{(k)}L_2^{(k)}, N_6^{(k)} = 4L_1^{(k)}L_3^{(k)},\\
&N_7^{(k)} = 4L_1^{(k)}L_4^{(k)}, N_8^{(k)} = 4L_2^{(k)}L_3^{(k)}, N_9^{(k)} = 4L_2^{(k)}L_4^{(k)}, N_{10}^{(k)} = 4L_3^{(k)}L_4^{(k)},
\end{aligned} \tag{23}$$

where $(L_j^{(k)}, j = 1, \cdots, 4)$ are the volume coordinates for the kth tetrahedron. $M_j^{(k)}$ and $N_j^{(k)}$ have the following properties

$$M_j^{(k)}(\mathbf{x}_i) = \delta_{ij}, \quad N_j^{(k)}(\mathbf{x}_i) = \delta_{ij}, \tag{24}$$

$$\sum_{j=1}^{4} M_j^{(k)}(\mathbf{x}) = 1, \quad \sum_{j=1}^{10} N_j^{(k)}(\mathbf{x}) = 1. \tag{25}$$

In the Galerkin finite element model, the weight functions are selected to be the same as the corresponding shape functions. Applying the finite element scheme (20) and (21) to each tetrahedron and using a standard procedure of the finite element method [33], we obtain a system of linear equations for the coefficients $\mathbf{u}_j$ and p_j on the whole mesh at t_{n+1}. Readers can refer to [3, 8] for detailed discussion about mixed finite element formulation for Navier-Stokes equations.

3.3. Stabilized finite element scheme

In order to circumvent the numerical instabilities of the Galerkin finite element method, we adopt the stabilization scheme proposed by Codina [6]. This scheme is capable of dealing with all the instabilities that the standard Galerkin method presents, namely the pressure instability, the instability arising from convection-dominated situation and the less popular instabilities found when the Navier-Stokes equations are dominated by the Coriolis force. For actual numerical computation in spheroidal geometry, we use a stabilized scheme that consists

of finding $\mathbf{u}^{n+1}$ and p^{n+1} such that

$$\begin{aligned}
&\int_V \left(\frac{3\mathbf{u}^{n+1}}{2\Delta t} + 2\hat{\mathbf{z}}\times\mathbf{u}^{n+1} + \nabla p^{n+1}\right)\cdot\mathbf{w}_\mathbf{u}\,\mathrm{d}V + \int_V E\nabla\mathbf{u}^{n+1}\cdot\nabla\mathbf{w}_\mathbf{u}\,\mathrm{d}V \\
&\quad + \sum_{k=1}^{\mathrm{Nel}}\int_{V^k}\tau_\mathbf{u}\left(2\hat{\mathbf{z}}\times\mathbf{w}_\mathbf{u} - E\nabla^2\mathbf{w}_\mathbf{u}\right)\cdot\left(\frac{3\mathbf{u}^{n+1}}{2\Delta t} + 2\hat{\mathbf{z}}\times\mathbf{u}^{n+1} + \nabla p^{n+1} - E\nabla^2\mathbf{u}^{n+1}\right)\mathrm{d}V \\
&\quad + \sum_{k=1}^{\mathrm{Nel}}\int_{V^k}\tau_p\left(\nabla\cdot\mathbf{w}_\mathbf{u}\right)\left(\nabla\cdot\mathbf{u}^{n+1}\right)\mathrm{d}V \\
&= \int_V\left(\frac{4\mathbf{u}^n - \mathbf{u}^{n-1}}{2\Delta t} + \mathbf{f}^{n+1} - \overline{\overline{\mathbf{u}^{n+1}\cdot\nabla\mathbf{u}^{n+1}}}\right)\cdot\mathbf{w}_\mathbf{u}\,\mathrm{d}V \qquad (26)\\
&\quad + \sum_{k=1}^{\mathrm{Nel}}\int_{V^k}\tau_\mathbf{u}\left(2\hat{\mathbf{z}}\times\mathbf{w}_\mathbf{u} - E\nabla^2\mathbf{w}_\mathbf{u}\right)\cdot\left(\frac{4\mathbf{u}^n - \mathbf{u}^{n-1}}{2\Delta t} + \mathbf{f}^{n+1} - \overline{\overline{\mathbf{u}^{n+1}\cdot\nabla\mathbf{u}^{n+1}}}\right)\mathrm{d}V \\
&\quad + \sum_{k=1}^{\mathrm{Nel}}\int_{V^k}\tau_p\left(\nabla\cdot\mathbf{w}_\mathbf{u}\right)g^{n+1}\,\mathrm{d}V,
\end{aligned}$$

$$\begin{aligned}
&\int_V\left(\nabla\cdot\mathbf{u}^{n+1}\right)w_p\,\mathrm{d}V + \sum_{k=1}^{\mathrm{Nel}}\int_{V^k}\tau_\mathbf{u}\nabla w_p\cdot\left(\frac{3\mathbf{u}^{n+1}}{2\Delta t} + 2\hat{\mathbf{z}}\times\mathbf{u}^{n+1} + \nabla p^{n+1} - E\nabla^2\mathbf{u}^{n+1}\right)\mathrm{d}V \\
&= \int_V g^{n+1}w_p\,\mathrm{d}V + \sum_{k=1}^{\mathrm{Nel}}\int_{V^k}\tau_\mathbf{u}\nabla w_p\cdot\left(\frac{4\mathbf{u}^n - \mathbf{u}^{n-1}}{2\Delta t} + \mathbf{f}^{n+1} - \overline{\overline{\mathbf{u}^{n+1}\cdot\nabla\mathbf{u}^{n+1}}}\right)\mathrm{d}V \qquad (27)
\end{aligned}$$

for all weight functions $\mathbf{w}_\mathbf{u}$ and w_p, where the parameters $\tau_\mathbf{u}$ and τ_p are computed within each element as

$$\tau_\mathbf{u} = \left[\frac{4E}{h^2} + \frac{2\left|\overline{\overline{\mathbf{u}^{n+1}}}\right|}{h} + |\Omega|\right]^{-1},$$

$$\tau_p = 4E + 2\left|\overline{\overline{\mathbf{u}^{n+1}}}\right|h + |\Omega|h^2,$$

where h is the element size and $\overline{\overline{\mathbf{u}^{n+1}}} = 2\mathbf{u}^n - \mathbf{u}^{n-1}$.

3.4. Scalable element-by-element (EBE) parallelization

We shall consider an implicit finite element scheme for time-dependent fluid dynamic problems in rotating spheroidal geometry. Let $Ax = b$ be the linear system resulted from the temporal and spatial discretization at each time step where A is the global coefficient matrix containing the physical parameters of a fluid dynamic model, x a column vector containing the unknown coefficients $\mathbf{u}_j$ and p_j as described in section 3.2.2, b a column vector. When the linear system $Ax = b$ is solved by a Krylov subspace method, the element-by-element (EBE) technique [1, 2, 19] can naturally parallelize a finite element computational code on a distributed memory, massively parallel computer by utilizing the fact that the coefficient matrix A is the sum of the element matrices A^e. The following discussion on the EBE technique used in our computations is intended to rely only on abstract features of the hardware and software environment and

should be applicable, in principle, to a variety of distributed memory, massively parallel systems. Our actual Fortran 90 implementation solves the linear system $Ax = b$ resulting from the finite element approximation (26) and (27) to the governing equations (9) and (12) by the BiCGstab(L) iterative solver [30, 22], with Message Passing Interface (MPI) as the communication tool. It not only achieves nearly ideal linear scalability on massively parallel computers but also is portable and does not require any support from other external numerical software packages.

We use two different distributed data structures to store the matrix A and vectors x and b. The central feature of the EBE parallelization strategy is that, in contrast to the classical finite element method (e.g., Zienkiewicz [33]), it avoids the typical assembly process and retains the global matrix A in the unassembled form. In other words, all element matrices A^e are stored and distributed evenly across different processors. Suppose the whole mesh consists of Nel elements (which are tetrahedrons in our case). The corresponding Nel element matrices A^e are distributed among NP processors such that

$$\mathrm{Nel} = \sum_{pe=1}^{\mathrm{NP}} \mathrm{Nel}_{pe} \tag{28}$$

where Nel_{pe} is the number of element matrices stored on processor pe. Note that the Nel_{pe}'s differ at most by one. This element-structure makes the formation of the element matrices embarrassingly parallel because the computations of A^e are independent of each other. The vector x (the same for b) is distributed in an equation-structure such that

$$\mathrm{Neq} = \sum_{pe=1}^{\mathrm{NP}} \mathrm{Neq}_{pe} \tag{29}$$

where Neq is the length of x and Neq_{pe} is the length of x_{pe} which is the segment of x stored on processor pe. Similarly, the Neq_{pe}'s differ also at most by one. By working on the element- and equation-structures, the EBE parallelization of the main algebraic operations, namely vector addition, inner product and matrix-vector multiplication, in an iterative procedure, is described in detail below.

The vector addition and inner product involve two vectors, say x and y, in the same equation-structure. The vector addition is naturally parallelized as

$$x + y \Longleftrightarrow x_{pe} + y_{pe} \text{ on all processors } pe = 1, 2, \cdots, \mathrm{NP}. \tag{30}$$

All additions, $x_{pe}+y_{pe}$, in (30) are componentwise operations on locally available data and thus no inter-processor communication is required. The inner product is a collective operation and thus requires inter-processor communication. The parallelization of an inner product $d = x \cdot y$ involves two steps:

(i) Evaluate local inner products $d_{pe} = x_{pe} \cdot y_{pe}$ on each processor pe;
(ii) Reduce (through communications) d from d_{pe}'s on all processors.

The parallelization of the most time-consuming matrix-vector product, say $v = Ax$, begins with computing the product in an EBE manner as

$$Ax = \left(\sum_{k=1}^{\mathrm{Nel}} A_k^e \right) x = \sum_{k=1}^{\mathrm{Nel}} A_k^e x_k^e = \sum_{k=1}^{\mathrm{Nel}} v_k^e = v, \tag{31}$$

where x_k^e and v_k^e represent the appropriate part of x and v associated with kth element and they are stored in a data structure conforming with element-structure. We parallelize the elementwise matrix-vector products in Eq. (31) as

$$\sum_{k=1}^{\mathrm{Nel}} A_k^e x_k^e = \sum_{pe=1}^{\mathrm{NP}} \sum_{k=1}^{\mathrm{Nel}_{pe}} A_k^e x_k^e = \sum_{pe=1}^{\mathrm{NP}} \sum_{k=1}^{\mathrm{Nel}_{pe}} v_k^e. \tag{32}$$

The parallel EBE matrix-vector multiplication can be summarized as

(i) Construct x_k^e from x (i.e., x_{pe}'s) for $k = 1, 2, \ldots, \mathrm{Nel}_{pe}$ on each processor pe;
(ii) Compute $v_k^e = A_k^e x_k^e$ for $k = 1, 2, \ldots, \mathrm{Nel}_{pe}$ on each processor pe;
(iii) Collect v_k^e's on all processors to form v (i.e., v_{pe}'s are updated).

Note that the second step involves data only in element-structure and thus it is communication free while the first and last steps require inter-processor communications because they exchange data between element- and equation-structures. The first step gathers information from equation-structure data x to construct element-structure data x_k^e's and the last step scatters element-structure data v_k^e's into equation-structure data v.

4. NUMERICAL RESULTS

4.1. Validation via the exact solution

For the verification of the accuracy and convergence of our finite element scheme (26) and (27), we consider the following test problem in a rotating fluid spheroid. A special external force $\mathbf{f}(\mathbf{x}, t)$, the Dirichlet boundary data $\boldsymbol{\psi}$ and the initial condition $\mathbf{u}^0$ are chosen such that an exact nonlinear solution, $\mathbf{u}_e$ and p_e, of the spheroidal system is given by

$$\mathbf{u}_e = \mathcal{S}(r, \theta, \phi) \cos 2\pi t \begin{pmatrix} 2r^2(4 + 5\cos 2\theta) \sin 2\phi \sin^2 \theta \\ 2r^2 \sin 2\phi \sin 4\theta \\ 8r^2 \cos 2\phi \cos^2 \theta \sin \theta \end{pmatrix}, \qquad \nabla \cdot \mathbf{u}_e \neq 0, \tag{33}$$

$$p_e = \mathcal{S}(r, \theta, \phi) \cos 2\pi t, \tag{34}$$

where (r, θ, ϕ) are spherical polar coordinates with $\theta = 0$ representing the axis of rotation and $\mathcal{S}$, in connection with the spheroidal domain, is defined as

$$\mathcal{S}(r, \theta, \phi) = (r \sin\theta \cos\phi)^2 + (r \sin\theta \sin\phi)^2 + \frac{(r \cos\theta)^2}{1 - \varepsilon^2} - 1$$

such that both $\mathbf{u}_e$ and p_e vanish on the bounding surface Σ of the spheroid.

The test problem is solved to study the spacial and temporal convergence of our numerical method by using the constructed exact nonlinear solution for rotating spheroidal systems. The following error norms (in both space and time) are used for the investigation of the convergence

$$\|\mathbf{u}^h - \mathbf{u}\| = \sqrt{\frac{1}{2V} \int_0^{t_{\max}} \int_V |\mathbf{u}^h - \mathbf{u}|^2 \, \mathrm{d}V \, \mathrm{d}t}\,, \tag{35}$$

$$\|p^h - p\| = \sqrt{\frac{1}{2V} \int_0^{t_{\max}} \int_V |p^h - p|^2 \, \mathrm{d}V \, \mathrm{d}t}\,, \tag{36}$$

Table I. Tetrahedral meshes employed in convergence tests ($h_0 = 0.85$).

Mesh size h	Unknowns	Tetrahedra	Nodes
h_0	495	160	309
$\approx h_0/2$	4,553	1,280	2,057
$\approx h_0/4$	39,349	10,240	14,993
$\approx h_0/8$	32,7661	81,920	114,465
$\approx h_0/16$	267,5165	655,360	894,529

where V denotes the volume of the spheroid. The discrete version of these norms, namely, $\|\mathbf{u}^h - \mathbf{u}\|_h$ and $\|p^h - p\|_h$, are obtained by approximating the integrations in space and time by the 4-point Gaussian quadrature and the trapezoidal rule, respectively. The tetrahedral mesh statistics employed in the convergence tests are listed in Table I.

We recall that, see, for example, [9], for all sufficiently smooth $\mathbf{u}$ and p at the time step t_{n+1}, there exist functions $\mathbf{u}^h$ and p^h, such that

$$\|\mathbf{u}^h - \mathbf{u}\|^{n+1} = \sqrt{\frac{1}{2V}\int_V |\mathbf{u}^h(\mathbf{r}, t_{n+1}) - \mathbf{u}(\mathbf{r}, t_{n+1})|^2 \, \mathrm{d}V} = O(h^2)\,, \tag{37}$$

$$\|p^h - p\|^{n+1} = \sqrt{\frac{1}{2V}\int_V |p^h(\mathbf{r}, t_{n+1}) - p(\mathbf{r}, t_{n+1})|^2 \, \mathrm{d}V} = O(h)\,. \tag{38}$$

Together with the second-order backward differentiation temporal discretization, we would expect

$$\|\mathbf{u}^h - \mathbf{u}\|_h = O(h^2 + \Delta t^2),$$
$$\|p^h - p\|_h = O(h + \Delta t^2)$$

numerically in our convergence tests.

We perform two convergence tests with different geometrical parameters $\varepsilon = 0.35$ and 0.70, all using a fixed Ekman number $E = 10^{-5}$. In each test, the error norms versus element size h and time step Δt are tabulated. Tables II and III demonstrate the accuracy and the convergence for the two tests with two different spheroids for $\varepsilon = 0.35$ and 0.70, respectively, being consistent with the theoretical prediction. An excellent agreement between the numerical nonlinear solutions and the constructed exact solution is achieved, validating our nonlinear spheroidal code in a comprehensive way.

4.2. Validation via special forced resonance

The primary aim is at providing a further validation by solving the governing equations (9) and (10) numerically subject to both a resonant forcing and the incompressible condition together with the experimental boundary condition $\mathbf{u}_\Sigma = 0$ on the bounding surface of a spheroid.

Before presenting the detailed numerical result, it is profitable to briefly discuss spheroidal polar coordinates (η, ϕ, τ), with the corresponding velocity $\mathbf{u} = (u_\eta, u_\phi, u_\tau)$, which will be needed for describing the forcing $\mathbf{f}$. For spheroidal geometry with eccentricity ε, the relationship

Table II. Convergence results for $\varepsilon = 0.35$ spheroid with $E = 10^{-5}$, $h_0 = 0.85$ and $\Delta t_0 = 0.01$.

h	Δt	$\|\mathbf{u}^h - \mathbf{u}\|_h$	ratios	$\|p^h - p\|_h$	ratios
h_0	Δt_0	6.332014E-3	——	1.940355E-2	——
$\approx h_0/2$	$\Delta t_0/2$	5.753727E-4	0.0909	1.702217E-2	0.8773
$\approx h_0/4$	$\Delta t_0/4$	4.455472E-5	0.0774	6.132294E-3	0.3603
$\approx h_0/8$	$\Delta t_0/8$	1.784173E-6	0.0400	1.909108E-3	0.3113
$\approx h_0/16$	$\Delta t_0/16$	2.563450E-7	0.1437	8.697255E-4	0.4556

Table III. Convergence results for $\varepsilon = 0.70$ spheroid with $E = 10^{-5}$, $h_0 = 0.85$ and $\Delta t_0 = 0.01$.

h	Δt	$\|\mathbf{u}^h - \mathbf{u}\|_h$	ratios	$\|p^h - p\|_h$	ratios
h_0	Δt_0	2.942919E-3	——	4.030963E-3	——
$\approx h_0/2$	$\Delta t_0/2$	2.603705E-4	0.0885	4.460741E-3	1.1066
$\approx h_0/4$	$\Delta t_0/4$	1.998087E-5	0.0767	1.770346E-3	0.3969
$\approx h_0/8$	$\Delta t_0/8$	7.621229E-7	0.0381	6.067633E-4	0.3427
$\approx h_0/16$	$\Delta t_0/16$	1.185576E-7	0.1556	3.097867E-4	0.5106

between rectangular Cartesian coordinates (x, y, z) and spheroidal polar coordinates (η, ϕ, τ) [35] is given by

$$x^2 = (\varepsilon^2 + \eta^2)(1 - \tau^2)\cos^2\phi, \tag{39}$$

$$y^2 = (\varepsilon^2 + \eta^2)(1 - \tau^2)\sin^2\phi, \tag{40}$$

$$z^2 = \eta^2\tau^2. \tag{41}$$

On the framework of spheroidal polar coordinates (η, ϕ, τ), the bounding surface of a spheroidal cavity Σ is then described by $\eta = \sqrt{1 - \varepsilon^2}$. Furthermore, the linearized equations (9) and (10) in spheroidal polar coordinates in the limits $E \to 0$ and $\mathbf{f} \to 0$, which describe non-dissipative inertial waves in a rotating spheroidal cavity, are

$$w\frac{\partial u_\eta}{\partial t} - 2\eta v u_\phi + u\frac{\partial p}{\partial \eta} = 0, \tag{42}$$

$$w\frac{\partial u_\tau}{\partial t} + 2\tau u u_\phi + v\frac{\partial p}{\partial \tau} = 0, \tag{43}$$

$$w\frac{\partial u_\phi}{\partial t} + 2(\eta v u_\eta - \tau u u_\tau) + \frac{w}{uv}\frac{\partial p}{\partial \phi} = 0, \tag{44}$$

$$uv\left[\frac{\partial}{\partial \eta}(w u u_\eta) + \frac{\partial}{\partial \tau}(w v u_\tau)\right] + w^2\frac{\partial u_\phi}{\partial \phi} = 0, \tag{45}$$

for which the boundary condition becomes

$$u_\eta = 0 \ \text{ at } \ \eta = \sqrt{1 - \varepsilon^2} \tag{46}$$

where

$$u=\sqrt{\eta^2+\varepsilon^2},\quad v=\sqrt{1-\tau^2},\quad w=\sqrt{\eta^2+\varepsilon^2\tau^2}. \tag{47}$$

Evidently, equations (42)–(45) allow us to write solutions $(\mathbf{u},p)$ in the form

$$(\mathbf{u},p)=[\mathbf{u}(\eta,\tau),p(\eta,\tau)]\exp\left[\mathrm{i}(m\phi+2\sigma t)\right]. \tag{48}$$

The elimination of the velocity $\mathbf{u}$ from equations (42)–(45) leads to the Poincaré equation for the pressure p, which can be written in spheroidal polar coordinates (η,ϕ,τ),

$$C_{\tau\tau}\frac{\partial^2 p}{\partial\tau^2}+C_{\eta\eta}\frac{\partial^2 p}{\partial\eta^2}+C_{\tau}\frac{\partial p}{\partial\tau}+C_{\eta}\frac{\partial p}{\partial\eta}+C_{\tau\eta}\frac{\partial^2 p}{\partial\tau\partial\eta}+C_0 p=0, \tag{49}$$

where

$$\begin{aligned}
C_{\tau\tau} &= \frac{v^2}{w^4}\left(\tau^2u^2+\frac{\sigma^2-1}{\sigma^2}\eta^2v^2\right),\\
C_{\eta\eta} &= \frac{u^2}{w^4}\left(\eta^2v^2+\frac{\sigma^2-1}{\sigma^2}\tau^2u^2\right),\\
C_{\tau} &= \frac{\tau}{w^6}\left[-2w^4+u^2v^2(3\eta^2-\tau^2\varepsilon^2)\right]+\\
&\quad \frac{\sigma^2-1}{\sigma^2}\left(\frac{v^2}{\tau w^6}\right)\left[w^4-\eta^2w^2(1+\tau^2)-2\eta^2\tau^2(u^2+\varepsilon^2v^2)\right],\\
C_{\eta} &= \frac{\eta}{w^6}\left[2w^4+u^2v^2(3\tau^2\varepsilon^2-\eta^2)\right]+\\
&\quad \frac{\sigma^2-1}{\sigma^2}\left(\frac{u^2}{\eta w^6}\right)\left[w^4-\tau^2w^2(\varepsilon^2-\eta^2)-2\eta^2\tau^2(u^2+\varepsilon^2v^2)\right],\\
C_{\tau\eta} &= -\frac{2\tau\eta u^2v^2}{\sigma^2w^4},\\
C_0 &= -\frac{m^2}{u^2v^2}.
\end{aligned}$$

The simplest non-axisymmetric solution to the Poincaré equation (49) describes equatorially antisymmetric inertial waves for which the pressure p is given by

$$p=\frac{(2m+1)!!}{2m!}u^mv^m\eta\tau\,\mathrm{e}^{\mathrm{i}(m\phi+2\sigma t)}, \tag{50}$$

where m denotes the azimuthal wavenumber of an inertial wave. With the availability of the explicit expression (50) for p, we can derive the velocity components by substituting (50) into equations (42)–(47) and then solving for $\mathbf{u}$, which yields

$$u_\eta=-\mathrm{i}\frac{(2m+1)!!}{4m!}\frac{\tau(uv)^m}{w}\left[\frac{-\eta^2m}{u(1-\sigma)}+\frac{u}{\sigma}\right]\mathrm{e}^{\mathrm{i}(m\phi+2\sigma t)}, \tag{51}$$

$$u_\phi=\frac{(2m+1)!!}{4m!}\,\frac{m\eta\tau}{(1-\sigma)}(uv)^{(m-1)}\mathrm{e}^{\mathrm{i}(m\phi+2\sigma t)}, \tag{52}$$

$$u_\tau=-\mathrm{i}\frac{(2m+1)!!}{4m!}\frac{\eta(uv)^m}{w}\left[\frac{\tau^2m}{v(1-\sigma)}+\frac{v}{\sigma}\right]\mathrm{e}^{\mathrm{i}(m\phi+2\sigma t)}. \tag{53}$$

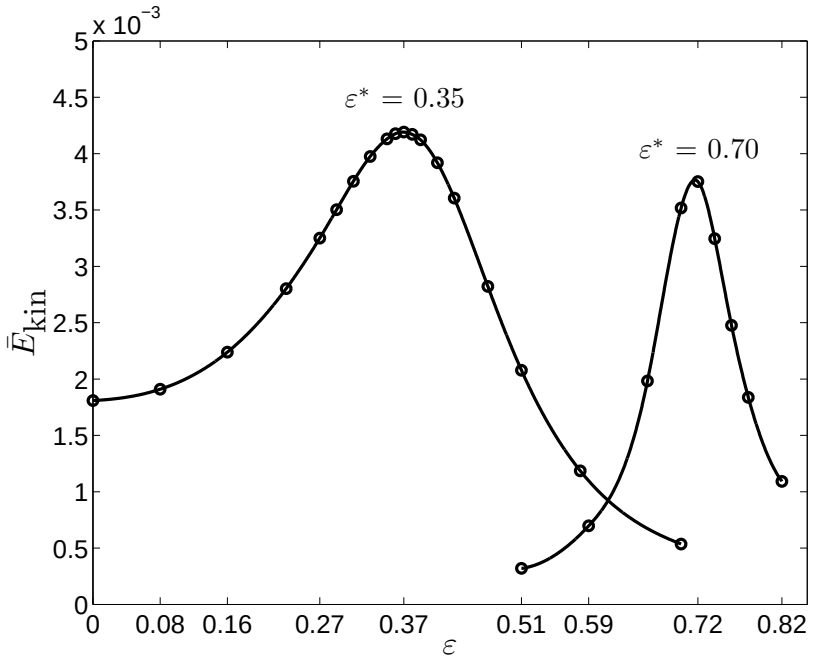

Figure 6. Mean kinetic energies $\bar{E}_{\rm kin}$ are shown as function of eccentricity ε for two fixed $\varepsilon^* = 0.35$ and $\varepsilon^* = 0.70$.

To determine the half-frequency σ of the inertial waves, we employ the boundary condition (46) on the envelope of the spheroidal cavity $\eta = \sqrt{1-\varepsilon^2}$, giving rise to the following simple dispersion relation

$$\sigma = \frac{1}{1+m(1-\varepsilon^2)}. \tag{54}$$

On substitution of (54) into (51)–(53) we obtain the three velocity components in closed form

$$u_\eta(m,\varepsilon,t) = -\mathrm{i}\frac{(2m+1)!![1+m(1-\varepsilon^2)]}{4m!}\frac{\tau(uv)^m}{w}\left[\frac{-\eta^2}{u(1-\varepsilon^2)}+u\right]\mathrm{e}^{\mathrm{i}(m\phi+2\sigma t)}, \tag{55}$$

$$u_\phi(m,\varepsilon,t) = \frac{(2m+1)!![1+m(1-\varepsilon^2)]}{4m!}\,\eta\tau(uv)^{(m-1)}\frac{1}{(1-\varepsilon^2)}\mathrm{e}^{\mathrm{i}(m\phi+2\sigma t)}, \tag{56}$$

$$u_\tau(m,\varepsilon,t) = -\mathrm{i}\frac{(2m+1)!![1+m(1-\varepsilon^2)]}{4m!}\frac{\eta(uv)^m}{w}\left[\frac{\tau^2}{v(1-\varepsilon^2)}+v\right]\mathrm{e}^{\mathrm{i}(m\phi+2\sigma t)}. \tag{57}$$

The simplest solution is obtained by setting $m = 1$ in (55)–(57), which is characterized by the vanishing of the radial flow in the spherical limit

$$u_\eta(\eta,\tau) \to 0 \ \text{ as } \ \varepsilon \to 0, \tag{58}$$

i.e., the fluid motion is purely toroidal in spherical geometry [24].

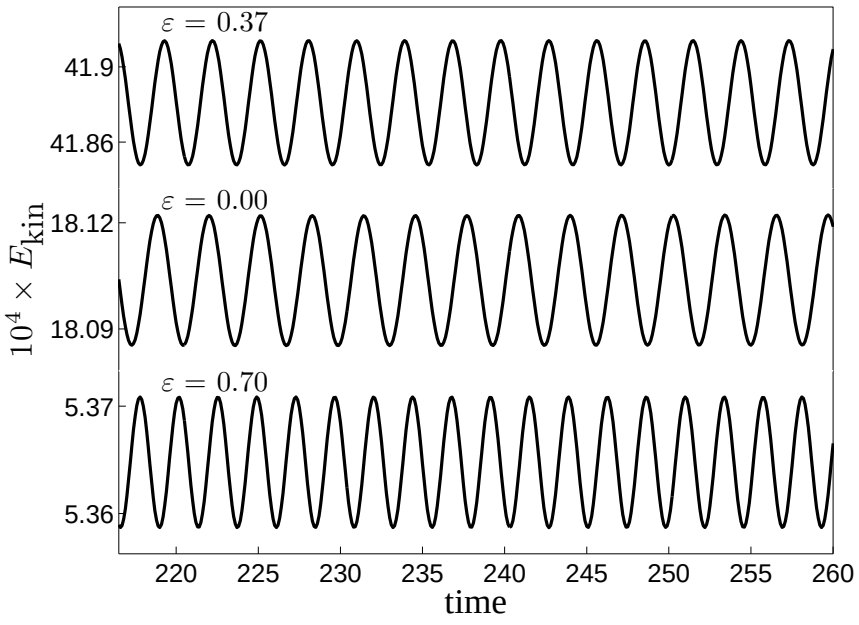

Figure 7. Kinetic energies $E_{\rm kin}(t)$ for three different eccentricities ε are shown as a function of time at a fixed $\varepsilon^* = 0.35$.

For a further validation of our spheroidal code, we choose the following parameterized, time-dependent forcing

$$\mathbf{f}(\mathbf{x}, \varepsilon^*, t) = [u_\eta, u_\phi, u_\tau]\,(m = 1, \varepsilon = \varepsilon^*, t) + c.c. \tag{59}$$

for the governing equations (9)–(10), where *c.c.* denotes the complex conjugate of the preceding term, and u_η, u_ϕ and u_τ are given by equations (55)–(57). By fixing the value of ε^* in the forcing $\mathbf{f}(\mathbf{x}, \varepsilon^*, t)$ while solving (9)–(10) for different spheroidal cavities marked by different eccentricities ε, we predict a resonant phenomenon in the following manner. When the eccentricity of a spheroidal container ε satisfies $|\varepsilon - \varepsilon^*|/\varepsilon^* \gg 1$ with $E \ll 1$, numerical solutions to the nonlinear equations (9)–(10) are characterized by small amplitudes; when ε satisfies $|\varepsilon - \varepsilon^*|/\varepsilon^* \ll 1$ with $E \ll 1$, however, the resonance takes place and, consequently, the amplitude of the forced numerical solutions reaches its maximum. For measuring the amplitude of the velocity $\mathbf{u}(\mathbf{r}, t)$, we introduce the kinetic energy of the time-dependent flow, $E_{\rm kin}(t)$, defined as

$$E_{\rm kin}(t) = \frac{1}{2V} \int_V |\mathbf{u}(\mathbf{r}, t)|^2 \, \mathrm{d}V, \tag{60}$$

and the mean kinetic energy $\bar{E}_{\rm kin}$ defined as

$$\bar{E}_{\rm kin} = \frac{1}{4\pi V} \int_0^{2\pi} \left[\int_V |\mathbf{u}(\mathbf{r}, t)|^2 \, \mathrm{d}V \right] \mathrm{d}t, \tag{61}$$

where V denotes the volume of the spheroidal container.

We have performed an extensive computation over a wide range of spheroids with different eccentricities at two given values of ε^*. In the first case, $\mathbf{f}$ is fixed by letting $m = 1$ and $\varepsilon^* = 0.35$ in (59) while we calculate nonlinear numerical solutions to the governing equations (9)–(10) at $E = 10^{-4}$ in different spheroids by changing its eccentricity from the spherical limit $\varepsilon = 0$ to a flatted spheroid with $\varepsilon = 0.7$. Fig. 6 shows the mean kinetic energies $\bar{E}_{\rm kin}$ as function of eccentricity ε at a fixed $\varepsilon^* = 0.35$. The kinetic energies $E_{\rm kin}(t)$ as a function of time are presented in Fig. 7 for three typical values of ε. Note that, if the nonlinear term in (9) is neglected at the limit $E \to 0$, it is theoretically predicted that $\bar{E}_{\rm kin} \to \infty$ when the eccentricity of a spheroid $\varepsilon \to 0.35$. This, of course, cannot occur in our numerical computations because the Ekman number E is finite and the nonlinear effect is fully included. The effects of the viscosity and nonlinearity not only limit the amplitude of the forced flow but also shift the resonant eccentricity from $\varepsilon = 0.35$ at $E \to 0$ to $\varepsilon = 0.37$ at $E = 10^{-4}$, as clearly indicated in Fig. 6. In the second case, we take the external forcing $\mathbf{f}$ by letting $m = 1$ and $\varepsilon^* = 0.7$ in (59), expecting that a rotating spheroid with its eccentricity ε satisfying $|\varepsilon - 0.7|/0.7 \ll 1$ would yield the largest amplitude. We have calculated many numerical solutions to the equations (9)–(10) with a fixed $\varepsilon^* = 0.7$ at $E = 10^{-4}$ for different spheroids ranging from $\varepsilon = 0.5$ to a highly flatted spheroid with $\varepsilon = 0.8$. The result of our numerical computation is also displayed in Fig. 6, showing the mean kinetic energies $E_{\rm kin}$ as function of ε at a fixed $\varepsilon^* = 0.7$. As a consequence of the viscosity and nonlinearity, the resonant eccentricity is shifted from the theoretical value $\varepsilon = 0.70$ at the limit $E \to 0$ to $\varepsilon = 0.72$ at $E = 10^{-4}$, which can be clearly seen in Fig. 6.

This satisfactory agreement between the theoretical prediction and the numerical simulations, which are performed over a wide range of different oblate spheroids, not only indicates the validity of our nonlinear spheroidal code but also suggests the flexibility of the code being capable of dealing with highly flatted spheroids.

5. Summary and remarks

As a consequence of rapid rotation, many planetary and astrophysical bodies are in the shape of an ablate spheroid. An efficient numerical method for computing nonlinear flows confined in an ablate spheroidal cavity has many applications for the problems of geophysical and astrophysical fluid dynamics. This paper presents an efficient EBE (Element-By-Element) finite element method that can be used to compute nonlinear flows confined in a rotating ablate spheroidal cavity with arbitrary eccentricity $0 \leq \varepsilon < 1$. We have placed the emphasis of our study on three different aspects of the numerical problem: the temporal and spatial tetrahedral discretization in a spheroidal cavity, the EBE parallelization scheme and the validation of the nonlinear spheroidal code. To authors' best knowledge, this paper represents the first study of applying the EBE finite element method to the problem of fluid dynamics in rotating spheroids with a wide range of geometric eccentricity.

A major difficulty in the numerical studies of rotating spheroidal fluids is how to comprehensively validate a complicated, lengthy nonlinear spheroidal code. We have chosen two different ways for the purpose of validation: by using the constructed exact solution and by invoking a special forcing that can theoretically cause the strong resonance in a rotating fluid spheroid marked by a particular value of eccentricity. A satisfactory agreement is achieved

between the constructed exact solution and the corresponding nonlinear numerical solution with an expected convergence property, representing, to a large extent, a comprehensive validation of the nonlinear spheroidal code. Moreover, a satisfactory agreement between the theoretical prediction and the nonlinear numerical solution over a wide range of oblate spheroids promises a wide application of the nonlinear code to various geophysical and astrophysical problems.

In summary, the parallel nature of the nonlinear spheroidal code, together with its high flexibility and its successful validation, opens an exciting new line of the numerical studies for precessionally-driven flows or tidally-driven flows in planets and stars in the era of modern massively parallel computers.

ACKNOWLEDGEMENTS

KHC is supported by Hong Kong RGC grant/700308, KZ is supported by UK NERC grant/G003548/1 and XL is supported by NSFC grant/10633030, STCSM/08XD14052, the CAS and 863-project grant/2006AA01A125. The parallel computation is supported by Shanghai Supercomputer Center.

REFERENCES

1. Behr M. Stabilized Finite Element Methods for Incompressible Flows with Emphasis on Moving Boundaries and Interfaces. *Ph.D. thesis, Department of Aerospace Engineering and Mechanics, University of Minnesota* 1992.
2. Behr M, Johnson A, Kennedy J, Mittal S, Tezduyar TE. Computation of incompressible flows with implicit finite element implementations on the Connection Machine. *Computer Methods in Applied Mechanics and Engineering* 1993; **108**:99–118.
3. Brezzi F, Fortin M. *Mixed and Hybrid Finite Element Methods.* Springer: Berlin, Heidelberg, 1991.
4. Bullard EC. The magnetic flux within the earth. *Proceedings of the Royal Society A* 1949; **197**:433–453.
5. Chan K, Zhang K, Li L, Liao X. A new generation of convection-driven spherical dynamos using EBE finite element method. *Physics of the Earth and Planetary Interiors* 2007; **163**:251–265.
6. Codina R. A nodal-based implementation of a stabilized finite element method for incompressible flow problems. *International Journal For Numerical Methods In Fluids* 2000; **33**:737–766.
7. Everett ME. A three-dimensional spherical mesh generator. *Geophysical Journal International* 1997; **130**:193–200.
8. Girault V, Raviart P. *Finite Element Approximation of the Navier-Stokes Equations.* Springer: New York, 1981.
9. Girault V, Raviart P. *Finite Element Methods for Navier-Stokes Equations: Theory and Algorithms.* Springer: Berlin, 1986.
10. Gubbins D, Roberts PH. Magnetohydrodynamics of the Earth's core. In *Geomagnetism*, vol. 2, Jacobs JA (eds), London: Academic Press, 1987; 1–183.
11. Hood P, Taylor C. Navier-Stokes equations using mixed-interpolation. In *Finite Element Methods in Flow Problems*, Oden JT, Zienkiewicz OC, Gallagher RH, Taylor C (eds). UAH Press: Huntsville, 1974; 57–66.
12. Glatzmaier GA, Roberts PH. A three-dimensional convective dynamo solution with rotating and finitely conducting inner core and mantle. *Physics of the Earth and Planetary Interiors* 1995; **91**:63–75.
13. Karniadakis GE, Israeli M and Orszag SA. High-order splitting methods for the incompressible Navier-Stokes equations. *Journal of Computational Physics* 1991; **97**:414–443.
14. Kress W, Lötstedt P. Time step restrictions using semi-explicit methods for the incompressible Navier-Stokes equations. *Computer Methods in Applied Mechanics and Engineering* 2006; **195**(33-36):4433–4447.
15. Lacaze L, Herreman W, Le Bars M, Le Dizs S, Le Gal P. Magnetic field induced by elliptical instability in a rotating spheroid. *Geophysical and Astrophysical Fluid Dynamics* 2006; **100**:299–317.
16. Liu A and Joe B. Quality local refinement of tetrahedral meshes based on 8-subtetrahedron subdivision. *Mathematics of Computation* 1996; **65**(215):1183–1200.
17. Lorenzani S, Tilgner A. Fluid instabilities in precessing spheroidal cavities. *Journal of Fluid Mechanics* 2001; **447**:111–128.

18. Malkus WVR. Precession of the earth as the cause of geomagnetism. *Science* 1968; **136**:259–264.
19. Margetts L. Parallel Finite Element Analysis. *Ph.D. Thesis, University of Manchester, UK* 2002.
20. Noir J, Cardin P, Jault D, Masson JP. Experimental evidence of non-linear resonance effects between retrograde precession and the tilt-over mode within a spheroid. *Geophysical Journal International*, 2003; **154**:407–416.
21. Persson PO, Strang G. A Simple Mesh Generator in MATLAB. *SIAM Review* 2004; **46**(2):329–345.
22. Sleijpen GLG, Fokkema DR. BiCGstab(L) for Linear Equations involving Unsymmetric Matrices with Complex Spectrum. *Electronic Transactions on Numerical Analysis* 1993; **1**:11–32.
23. Peterson DM, Hummel CA, Pauls TA, Armstrong JT, Benson JA, Gilbreath GC, Hindsley RB, Hutter DJ, Johnston KJ, Mozurkewich D, Schmitt HR. Vega is a rapidly rotating star. *Nature* 2006; **440**:896–899.
24. Roberts PH, Stewartson K. On the motion of a liquid in a spheroidal cavity of a precessing rigid body: II. *Mathematical Proceedings of the Cambridge Philosophical Society*, 1965; **61**:279–288.
25. Sarson GR, Jones CA. A convection driven geodynamo reversal model. *Physics of the Earth and Planetary Interiors* 1999; **111**:3–20.
26. Schmitt D. Numerical study of viscous modes in a rotating spheroid. *The Journal of Fluid Mechanics* 2006; **567**:399-414.
27. Stewartson K, Roberts PH. On the motion of a liquid in a spheroidal cavity of a precessing rigid body. *The Journal of Fluid Mechanics* 1963; **17**:1–20.
28. Tilgner A. Kinematic dynamos with precession driven flow in a sphere. *Geophysical and Astrophysical Fluid Dynamics* 2007; **100**:1–9.
29. Tilgner A. Precession driven dynamos *Physics of Fluids* 2005; **17**:034104.
30. van der Vorst HA. BiCGSTAB: A fast and smoothly converging variant of Bi-CG for the solution of nonsymmetric linear systems. *SIAM Journal on Scientific Computing* 1992; **13**:631–644.
31. Vanyo JP, Wilde P, Cardin P, Olson P. Experiments on precessing flows in the Earth's liquid core. *Geophysical Journal International* 1995; **121**:136–142.
32. Walker MR, Barenghi CF. High resolution numerical dynamos in the limit of a thin disk galaxy. *Geophysical and Astrophysical Fluid Dynamics* 1994; **76**:265–281.
33. Zienkiewicz OC. *The finite element method* (3rd edn). McGraw-Hill: London, 1977.
34. Zhang K, Busse F. Convection driven magnetohydrodynamic dynamos in rotating spherical shells. *Geophysical and Astrophysical Fluid Dynamics* 1989; **49**:97–116.
35. Zhang K, Liao X, Earnshaw P. On inertial waves and oscillations in a rapidly rotating fluid spheroid. *The Journal of Fluid Mechanics* 2004; **504**:1–40.